

## Near-field flow features of underexpanded microjets emerging from a rectangular convergent nozzle with a high-aspect-ratio

Shota Yoshimi, Takahiro Yamashita<sup>1</sup>, Shinichiro Nakao<sup>1</sup>, Yoshiaki Miyazato<sup>ID, \*,1</sup>

*Department of Mechanical Systems Engineering, The University of Kitakyushu, 1-1 Hibikino, Wakamatsu-ku, Kitakyushu, 808-0135, Japan*

### ARTICLE INFO

**Keywords:**

Density measurement  
Mach-Zehnder tomography  
RANS prediction  
Rectangular nozzle  
Shock wave  
Underexpanded microjet

### ABSTRACT

Underexpanded microjets emerging from a rectangular convergent nozzle with an aspect ratio of 10 at the exit face are quantitatively visualized via Mach-Zehnder tomography (MZT) with the finite-fringe setting. Multiview interferograms around the central axis of the microjet are taken at a nozzle pressure ratio (NPR) of 4.0. The Reynolds number based upon the height in the minor-axis plane and flow properties at the nozzle exit is  $1.74 \times 10^4$ . Fourier fringe analysis is utilized to extract the phase shifts between the background fringe and deformed fringe patterns. The density fields of the microjets are subsequently reconstructed via the convolution back-projection (CBP) method. Near-field flow features of the microjets are demonstrated with the isopycnic surface as well as the density contour plots in the minor-axis and major-axis planes. In addition, microjets issuing from the nozzle with the same geometry as in the experiment are solved via the Reynolds-averaged Navier-Stokes (RANS) equations with Menter's shear stress transport (SST)  $k-\omega$  turbulence model for mutual comparison with the experimental results. The streamwise density profiles along the jet centerline as well as the liplines in the minor-axis and major-axis planes are quantitatively compared between the experimental and simulation results. Shock structures and topology showing the streamwise evolution of a shock system in a high-aspect-ratio rectangular microjet are experimentally clarified for the first time with a high spatial resolution of approximately 5.0  $\mu\text{m}$ .

### 1. Introduction

Supersonic microjets emerging from rectangular nozzles with high aspect ratios have been widely used because of their practical application in mechanical devices such as gas wiping in continuous steel strip galvanizing lines [1] and air knives in next-generation solar cell manufacturing processes [2,3]. Continuous galvanizing is a process in which the surface of a continuous strip of steel is coated on both sides with a thin layer of zinc. The coating, which is applied by passing the strip through a zinc bath at high temperatures, improves the corrosion resistance of the finished product. Gas wiping jets are used in the process to control the final coating weight applied to the substrate. The wiping process is one of the factors limiting the maximum line speed of continuous galvanizing lines. On the other hand, jets emerging from a rectangular nozzle with a narrow gap are sometimes called air knives. Air knives play a very important role in the manufacturing process of perovskite solar cells [2–4] by using high-speed gas jets to uniformly dry the surface of the deposited perovskite layer. This improves the quality and performance of the perovskite layer and

the overall efficiency of the solar cell. The use of air knives in the production of perovskite solar cells is key to achieving efficient and economical production. Given the pressure conditions across the air knife nozzle described in the literature, the flows exiting the air knife nozzle appear to be underexpanded jets. However, few studies have been conducted on underexpanded microjets issuing from large aspect ratio rectangular nozzles, even though it is very important to know the physical properties of planar microjets to improve work efficiency.

Kashimura et al. [5] solved the Reynolds-averaged Navier-Stokes (RANS) equations with a compressible  $k-\epsilon$  turbulence model of microjets issuing from a two-dimensional convergent nozzle with a height of 1 mm at the exit. The nozzle pressure ratio (NPR) defined as the ratio  $p_{os}/p_b$  of the plenum pressure  $p_{os}$  to the back pressure  $p_b$  was varied over a range of NPRs from 1.893 to 6.0 to investigate underexpanded sonic jet structures and shock cell spacings. Handa et al. [6] applied molecular tagging velocimetry (MTV) for supersonic microjets issuing from a convergent-divergent nozzle with a design Mach number of 2.0 and a rectangular shape of 500  $\mu\text{m} \times 5000 \mu\text{m}$  (AR = 10: the

\* Corresponding author.

E-mail addresses: [acaddress443@gmail.com](mailto:acaddress443@gmail.com) (S. Yoshimi), [yamalab193@gmail.com](mailto:yamalab193@gmail.com) (T. Yamashita), [s-nakao@kitakyu-u.ac.jp](mailto:s-nakao@kitakyu-u.ac.jp) (S. Nakao), [miyazato@kitakyu-u.ac.jp](mailto:miyazato@kitakyu-u.ac.jp) (Y. Miyazato).

<sup>1</sup> These authors contributed equally to this work.

aspect ratio of the major dimension to the minor dimension at the nozzle exit). They clarified the effects of the Reynolds number on the microjet structure including the supersonic length and velocity decay process. Aniskin et al. [7,8,9] measured the Pitot pressures along the central axis of free jets issuing from flat convergent micronozzles with heights ranging 175  $\mu\text{m}$  to 22.3  $\mu\text{m}$  and corresponding ARs ranging 22 to 116. They acquired the main parameters including shock-cell spacing and supersonic length and investigated the effects of Pitot microtube diameter on the main parameters. Two convergent nozzles with sizes of 22.3  $\mu\text{m} \times 2593 \mu\text{m}$  (AR = 116) and 83.3  $\mu\text{m} \times 3823 \mu\text{m}$  (AR = 46) and two glass Pitot tubes with inner diameters ( $\mu\text{m}$ )/outer diameters ( $\mu\text{m}$ ) of 24/70 and 16/42 were used in the experiments. The experimental results demonstrated that the length of the first shock-cell measured by the Pitot microtube is overestimated in comparison with that visualized by the shadowgraph method, but the Pitot tube diameter has a minor effect on the supersonic length. Handa [10] focused on the collapse length of slightly underexpanded microjets, which is defined as the distance from the nozzle exit to the location in the flow direction where the jet spreads abruptly. The microjets were discharged from a rectangular convergent nozzle of 500  $\mu\text{m}$  high and 5000  $\mu\text{m}$  wide at the exit and visualized via planar laser-induced fluorescence (PLIF) and molecular tagging velocimetry (MTV) techniques. Most recently, Yoshimi et al. [11] numerically investigated the three-dimensional structure of an underexpanded microjet issuing from a rectangular convergent nozzle with AR = 10 under the condition of NPR = 5 and demonstrated the shock structures of the near-field region of the first shock-cell. However, the numerical calculations were validated only by qualitative comparison with schlieren photographs, because little is experimentally known about the shock structures in the near-field region of planar microjets.

The insertion of an intrusive probe into shock-dominated flows causes a significant change in the flow field, which naturally leads to nonnegligible errors in the obtained measurement values. In the case of velocity measurement techniques using tracer particles, such as laser Doppler anemometry (LDA), and particle image velocimetry (PIV), entrained particles do not follow the flow immediately after the shock wave, which is referred to as velocity slip error ([12–14]). On the other hand, background oriented schlieren (BOS) [15] and rainbow schlieren deflectometry (RSD) [16,17], which have been developed as quantitative optical visualization techniques for supersonic flows, require intricate integration operations to obtain density fields because the acquired data are related to the density gradient of the flow. In our study, an underexpanded microjet emerging from a rectangular convergent nozzle with a high aspect ratio is quantitatively visualized via Mach-Zehnder interferometry with computer tomography (MZT).

## 2. Experimental methods

### 2.1. Measurement systems and test nozzle

A schematic drawing of the experimental setup is shown in Fig. 1. The experiment is performed in an intermittent blowdown compressible air facility with MZT. Ambient air is pressured by a compressor up to 20 MPa, and then stored in a high-pressure reservoir with a capacity of 5  $\text{m}^3$  after being filtered and dried. The supply line from the reservoir can be connected to the plenum chamber through coupling, as shown in Fig. 1. Hence, the high-pressure dry air from the reservoir stagnates in the plenum chamber and is then discharged into the atmosphere through a test nozzle. In the present experiment, the back pressure  $p_b$  (=atmospheric pressure) is 100 kPa  $\pm$  0.5 kPa. The total temperature in the plenum chamber is equal to the room temperature ( $T_b = 300 \text{ K} \pm 0.1 \text{ K}$ ). Quantitative optical observations of jet flow fields are carried out via MZT at a nozzle pressure ratio of 4.0 to produce shock-dominated flows.

As shown in Fig. 2, a convergent nozzle with a rectangular cross-section of  $h = 0.3 \text{ mm}$  in height by  $w = 3 \text{ mm}$  in width at the exit

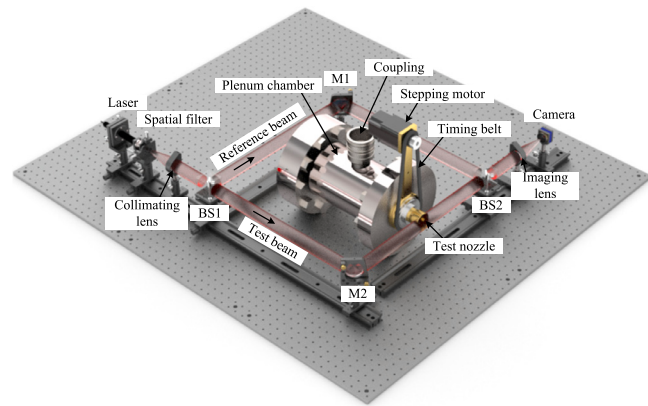


Fig. 1. Schematic drawing of the intermittent blowdown compressed air facility with a Mach-Zehnder interferometer optical system.

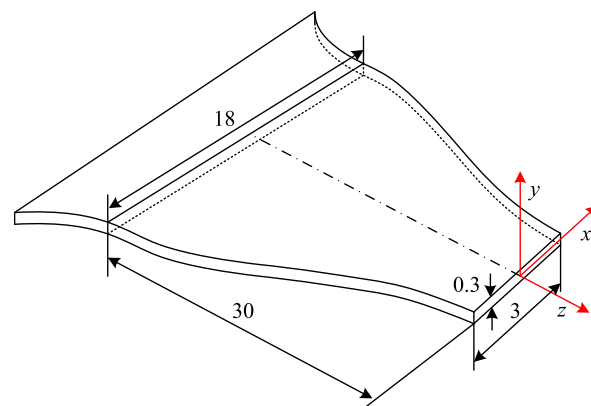


Fig. 2. Cut model of a rectangular convergent nozzle with a Cartesian coordinate system ( $x$ ,  $y$ ,  $z$ ) with all dimensions in mm.

face is used as the test nozzle. The aspect ratio AR ( $= w/h$ ) equals 10. The nozzle wall contour in the major-axis plane from the nozzle inlet to the exit is designed by a sinusoidal curve to provide smooth uniform flows at the nozzle inlet and exit. The height of the nozzle remains constant at 0.3 mm over the entire length from the nozzle inlet to the exit. The Cartesian coordinate system ( $x$ ,  $y$ ,  $z$ ) is employed with its origin at the center of the nozzle exit plane; the  $x$ -,  $y$ -, and  $z$ -axes are oriented along the directions of the major-axis, minor-axis, and jet central-axis, respectively. The Reynolds number based on the height ( $h = 0.3 \text{ mm}$ ) in the minor-axis plane and flow properties at the nozzle exit is  $1.74 \times 10^4$ .

### 2.2. Mach-Zehnder interferometry

A Helium-Neon (He-Ne) laser (Sigma Koki, model 05-LHP-925), characterized by a wavelength of 632.8 nm, an output power of 5 mW, and a beam diameter of 0.48 mm, is employed as the light source of the Mach-Zehnder interferometer. As shown in Fig. 1, the light beam issuing from the He-Ne laser passes through a special filter and a collimating lens to form a parallel beam, which is split into reference and test beams by a beam splitter BS1. The reference and test beams are reflected by plane mirrors M1 and M2, respectively, interact again with another beam splitter BS2, and then pass through an imaging lens to reach the recording medium of a camera.

Mach-Zehnder interferometry for obtaining density fields can be broadly classified into infinite-fringe and finite-fringe settings [18]. In the former setting, the phase difference between the reference and test beams reaching the recording medium in the absence of flow must be

zero, making adjusting the optical system difficult. Furthermore, the former setting has lower spatial resolution than the latter setting does and requires prior knowledge of the direction of increase or decrease in density. Therefore, the present Mach-Zehnder system uses the finite-fringe setting, which adjusts the optics to produce parallel interference fringes on the recording medium when there is no flow.

### 3. Reconstruction of jet density fields

#### 3.1. Wave interference between the reference and test beams

When the test beam passes through a free jet with a variable refractive-index field, the background fringes are changed into deformed fringe patterns. As shown in Fig. 3, for simplicity, we first consider the reference and test beams after the beams pass through BS2 (see Fig. 1) as plane waves. The coordinate  $x$  is the direction of the optical axis, in which the test beam propagates after being reflected at M2 as shown in Fig. 1. The coordinates  $y$  and  $z$  form the vertical plane perpendicular to the  $x$  direction. The reference beam  $\Psi_1$  travels in the direction rotated at an angle  $\eta$  around the  $y$ -axis relative to the  $x$ -axis, and the test beam  $\Psi_2$  without flow in the test section propagates in the positive direction of the  $x$  axis.

If the reference and test beams have the same phase  $\varphi_0$  at  $z = t = 0$  without being influenced by the refractive index fields, they can be expressed for a fixed  $y = y_0$  as follows:

$$\Psi_1(\mathbf{r}, t) = a \exp \{i(\mathbf{k}_1 \cdot \mathbf{r} - \omega t + \varphi_0)\} \quad (1)$$

$$\Psi_2(\mathbf{r}, t) = a \exp \{i(\mathbf{k}_2 \cdot \mathbf{r} - \omega t + \varphi_0)\} \quad (2)$$

where  $\omega$  and  $a$  are the angular frequency and amplitude of light in still air, respectively and where  $t$  is the time.  $\mathbf{k}_1$  and  $\mathbf{k}_2$  are the wave vectors, and  $\mathbf{r}$  is the position vector. They are given by

$$\mathbf{k}_1 = \frac{2\pi}{\lambda_a} (\cos \eta, 0, -\sin \eta), \quad \mathbf{k}_2 = \frac{2\pi}{\lambda_a} (1, 0, 0), \quad \mathbf{r} = (x, y_0, z) \quad (3)$$

where,  $\lambda_a$  is the wavelength of light in still air. As shown in Fig. 3(d), if the test wave experiences a path difference  $d = d(y_0, z)$  in propagation distance through changes in the refractive index, the resultant test wave  $\Psi'_2$  becomes

$$\Psi'_2(\mathbf{r}, t) = a \exp \left[ i \left( \mathbf{k}_2 \cdot \mathbf{r} - \omega t + \varphi_0 - \frac{2\pi}{\lambda_a} d \right) \right] \quad (4)$$

If  $\Psi_1$  and  $\Psi_2$  are superimposed on a recording medium located at  $x = 0$ , the resultant intensity field can be expressed as

$$g_r(y_0, z) \equiv |\Psi_1(\mathbf{r}, t) + \Psi_2(\mathbf{r}, t)|^2 \\ = 2a^2 + 2a^2 \cos [(\mathbf{k}_2 - \mathbf{k}_1) \cdot \mathbf{r}] \quad (5)$$

This intensity varies in a sinusoidal form. Therefore, there are local maxima under the following conditions.

$$(\mathbf{k}_2 - \mathbf{k}_1) \cdot \mathbf{r} = 2m\pi \quad (6)$$

where  $m$  is an integer.

Substitution of Eq. (3) into Eq. (6) leads to

$$z = z_m = \frac{m\lambda_a}{\sin \eta} \quad (7)$$

This implies that the intensity distribution has the maximum brightness at the locations of  $z = z_m$ .

Using Eq. (7), the interval  $b$  between interferograms on the medium ( $x = 0$ ) is given by:

$$b = |z_{m+1} - z_m| = \frac{\lambda_a}{\sin \eta} \quad (8)$$

The interval  $b$  becomes narrower with increasing  $\eta$  for  $0 < \eta < \pi/2$ , and it shows infinite fringe patterns for  $\eta = 0$ .

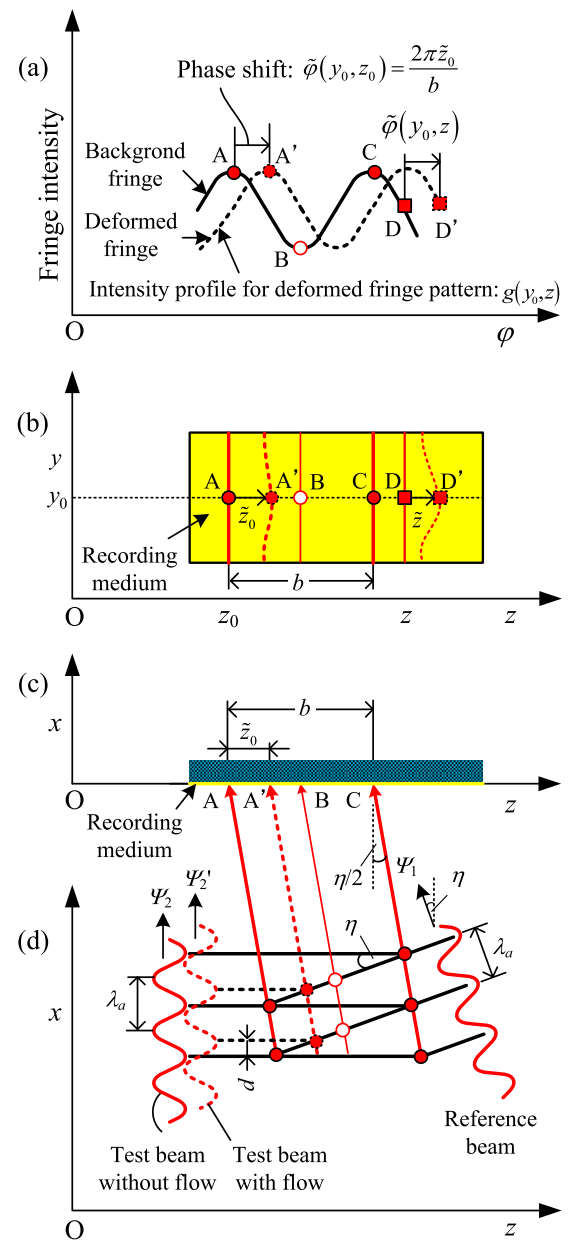


**Fig. 3.** Variation in background and deformed fringes by the finite-fringe setting with (a) fringe intensity profiles at  $y = y_0$ , (b) fringe patterns on the recording medium, (c) incidence of reference and test beams into the recording medium, and (d) wave interference between the reference and test beams at  $y = y_0$ .

Similarly, from Eqs. (1) and (4), the intensity field experiencing changes in the refractive index is given by

$$g(y_0, z) = |\Psi_1(\mathbf{r}, t) + \Psi'_2(\mathbf{r}, t)|^2 \\ = 2a^2 + 2a^2 \cos \left[ (\mathbf{k}_2 - \mathbf{k}_1) \cdot \mathbf{r} - \frac{2\pi}{\lambda_a} d \right] \quad (9)$$

A comparison of Eqs. (5) and (9) shows that  $g(y_0, z)$  can be translated into a phase:

$$\tilde{\varphi}(y_0, z) = \frac{2\pi}{\lambda_a} d \quad (10)$$

or it can be converted into the corresponding path difference

$$\tilde{z} = \frac{b\tilde{\varphi}(y_0, z)}{2\pi} \quad (11)$$

as shown in Fig. 3(b) and (c).

Substitution of Eq. (3) into Eq. (9) and considering Eq. (10) yields

$$g(y_0, z) = 2a^2 + 2a^2 \cos [k_0 z - \tilde{\varphi}(y_0, z)] \quad (12)$$

on the recording medium where  $k_0 = 2\pi/b$ .

### 3.2. Fourier transform method

Background and deformed fringe patterns taken via a digital camera are illustrated in Fig. 3(a) and (b) as lines of constant phase at  $y = y_0$ . The parallel and equally spaced fringes shown as red solid lines in Fig. 3(b) are also referred to as wedge fringes. The interval  $b$  in Fig. 3(b) denotes the distance between two successive crests of the background fringes, and it is a function of the intersection angle ( $\eta$ ) between the reference and test beams and the wavelength ( $\lambda_a$ ) of the laser light used in the experiment, as shown in Eq. (8). The black dashed line in Fig. 3(a) shows the intensity profile  $g(y_0, z)$  corresponding to the deformed fringe pattern at a particular vertical position  $y_0$ , which can be given [19,20] by

$$g(y_0, z) = g_0(y_0, z) + g_1(y_0, z) \cos [k_0 z - \tilde{\varphi}(y_0, z)] \quad (13)$$

In this expression,  $g_0(y_0, z)$  and  $g_1(y_0, z)$  are used instead of  $a^2$  in the first and second terms on the right-hand side (see Eq. (12)). The phase shift  $\tilde{\varphi}(y_0, z)$  contains only the desired information on the density field in the free jet. The intensity profile of the deformed fringe pattern expressed as Eq. (13) can be rewritten in the following expression:

$$g(y_0, z) = g_0(y_0, z) + c(y_0, z) \exp (ik_0 z) + c^*(y_0, z) \exp (-ik_0 z) \quad (14)$$

with

$$c(y_0, z) = \frac{1}{2} g_1(y_0, z) \exp [-i\tilde{\varphi}(y_0, z)] \quad (15)$$

where,  $i$  is the imaginary unit and the asterisk  $*$  denotes the complex conjugate.

The Fourier transform of Eq. (14) with respect to  $z$  is given by:

$$G(y_0, k) = G_0(y_0, k) + C(y_0, k - k_0) + C^*(y_0, k + k_0) \quad (16)$$

where the capital letters denote the Fourier transforms of the respective primitive functions and where  $k$  is the spatial wavenumber in the  $z$  direction. Since the spatial variations in  $g_0(y_0, z)$ ,  $g_1(y_0, z)$ , and  $\tilde{\varphi}(y_0, z)$  are slow compared with the spatial frequency  $k_0$  when the interval between fringes is sufficiently small, the Fourier spectra in Eq. (16) are separated by the wavenumber  $k_0$  and have three independent peaks, as schematically shown in Fig. 4(a). We make use of either of these two spectra on the carrier, e.g.,  $C(y_0, k - k_0)$ , and translate it by  $k_0$  on the wavenumber axis toward the origin to obtain  $C(y_0, k)$  as shown in Fig. 4(b). The unwanted background variation  $G_0(y_0, k)$  is filtered out in this stage by the pertinent bandpass filter.

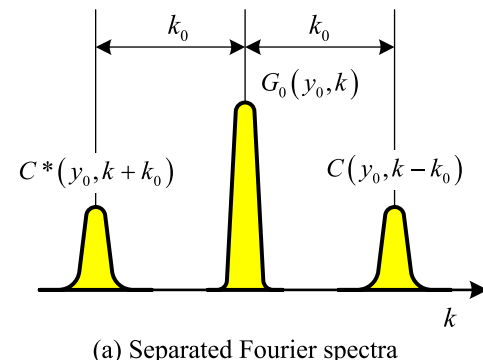
Applying the inverse Fourier transform of  $C(y_0, k)$  with respect to  $k$  to obtain  $c(y_0, z)$  and taking the logarithm of Eq. (15) leads to

$$\ln c(y_0, z) = \ln \frac{g_1(y_0, z)}{2} - i\tilde{\varphi}(y_0, z) \quad (17)$$

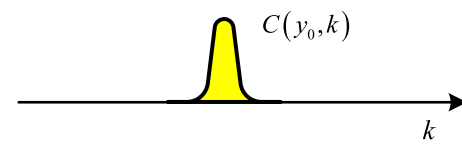
Consequently, the phase shift  $\tilde{\varphi}(y_0, z)$  in the imaginary part of Eq. (17) can be completely separated from the unwanted amplitude variation  $g_1(y_0, z)$  in the real part.

### 3.3. Convolution back projection method

Fig. 5 shows a light ray traveling in the jet cross-section ( $x$ - $y$  plane) at a fixed streamwise location of an asymmetric jet emerging from a test nozzle and the phase shift from the original location of an interferogram on a recording medium where the  $x$ ,  $y$ ,  $z$  rectangular Cartesian coordinate system is used and the  $z$ -axis is parallel to the streamwise direction, which is also perpendicular to the  $x$ ,  $y$  plane. The refractive index field or density field is investigated for a cross-section with a constant  $z$ . Accordingly, we omit the independent variable  $z$  in the subsequent analysis to reconstruct two-dimensional density fields.



(a) Separated Fourier spectra



(b) Parallel translation of single spectrum selected

Fig. 4. Fourier transform method for fringe pattern analysis with (a) separated Fourier spectra and (b) parallel translation of a single selected spectrum.

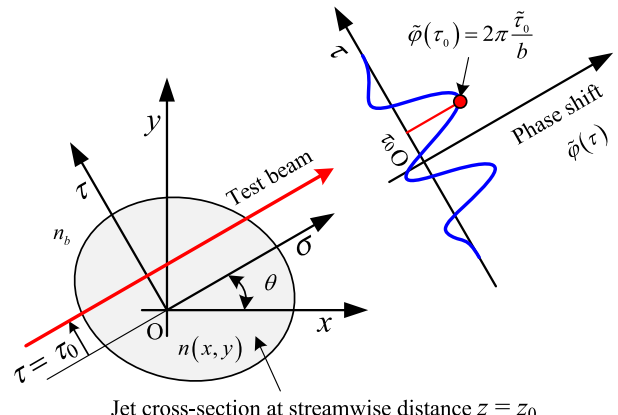


Fig. 5. Light beam passing through an asymmetric refractive index field with (a) an asymmetric refractive index field and (b) a phase shift profile at a fixed  $z$ .

As shown in Fig. 5, let us consider the rotated coordinates  $(\sigma, \tau)$  inclined at an angle  $\theta$  away from the fixed-original coordinates  $(x, y)$  where  $n(x, y)$  and  $n_b$  in Fig. 5 indicate the refractive indices in the jet cross-section and that of the surrounding air, respectively. Then, for a light ray traveling in the  $\sigma$  direction with an offset of  $\tau$  from the axis  $\sigma$ , the optical path difference  $\Lambda_\theta$  of the test beam, which passes through the field with and without the jet, can be expressed by the Radon transform with the Dirac  $\delta$ -function:

$$\Lambda_\theta(\tau) = \int_{-\infty}^{\infty} \int_{-\infty}^{\infty} \tilde{n}(x, y) \delta(x \sin \theta - y \cos \theta + \tau) dx dy \quad (18)$$

where  $\tilde{n}(x, y) \equiv n(x, y) - n_b$ . The optical path difference  $\Lambda_\theta$  is taken for a range of various angles from  $\theta = 0$  deg to 180 deg. The task of tomographic reconstruction in the present investigation is to find  $\tilde{n}(x, y)$  based upon a given knowledge of  $\Lambda_\theta$  and then density fields can be obtained through a well-known linear relation between the refractive index and density, as described later.

The transfer from the  $(x, y)$  to  $(\sigma, \tau)$  coordinate systems for the integral of the right-hand side of Eq. (18) leads to

$$\Lambda_\theta(\tau) = \int_{-\infty}^{\infty} \tilde{n}(\sigma \cos \theta - \tau \sin \theta, \sigma \sin \theta + \tau \cos \theta) d\sigma \quad (19)$$

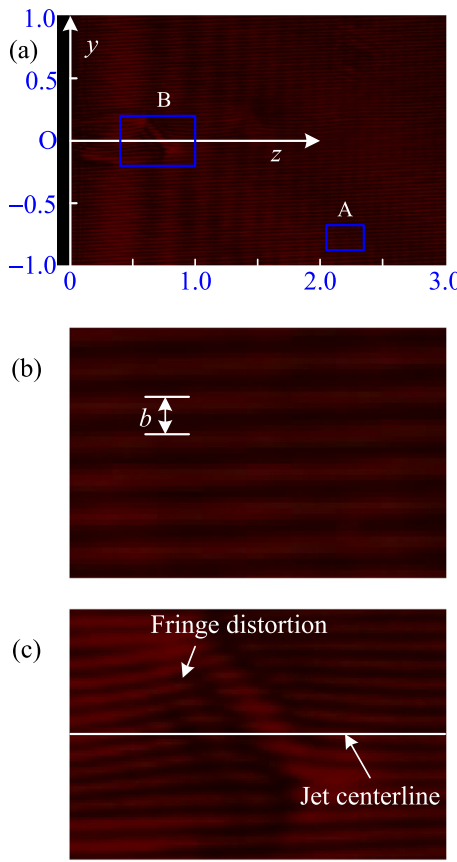


**Fig. 6.** Interferogram image of a rectangular underexpanded microjet at  $\text{NPR} = 4.0$  and  $\theta = 0^\circ$  with (a) the whole field of view, (b) the enlarged view of Part A, and (c) the enlarged view of Part B. The Mach-Zehnder interferometer was set up such that the wavefront direction of the background interference fringes is perpendicular to the  $z$ -axis.

After the one-dimensional Fourier transform of Eq. (19) with respect to the  $\tau$  variable and the use of the transform from the  $(\sigma, \tau)$  to  $(x, y)$  coordinate systems, it reduces to the following relation:

$$\begin{aligned} \mathcal{F}(\Lambda_\theta(\tau)) &\equiv \int_{-\infty}^{\infty} \Lambda_\theta(\tau) \exp(-2\pi i \tau \zeta) d\tau \\ &= \int_{-\infty}^{\infty} \int_{-\infty}^{\infty} \tilde{n}(x, y) \exp[-2\pi i(ux + vy)] dx dy \end{aligned} \quad (20)$$

with  $u = -\zeta \sin \theta$  and  $v = \zeta \cos \theta$ .

The right-hand side of Eq. (20) expresses the two-dimensional Fourier transform of  $\tilde{n}(x, y)$ . Hence, the inverse Fourier transform of Eq. (20) with  $u = -\zeta \sin \theta$  and  $v = \zeta \cos \theta$  and after some rearrangement, it reduces to

$$\tilde{n}(x, y) = \int_0^\pi \left\{ \int_{-\infty}^{\infty} |\zeta| \mathcal{F}(\Lambda_\theta(\tau)) \exp(2\pi i \tau \zeta) d\zeta \right\}_{\tau=-x \sin \theta + y \cos \theta} d\theta \quad (21)$$

The shift magnitude  $\tilde{\tau}$  of the deformed fringe relative to the background fringe at a fixed location (constant  $\tau$ ) on the recording medium can be given by

$$\tilde{\tau} = b \frac{\Lambda_\theta(\tau)}{\lambda_0} \quad (22)$$

where  $b$  is the wavelength of the background fringes and where  $\lambda_0$  is the wavelength of the light in vacuum for the laser used in the experiment.

The phase shift  $\tilde{\varphi}_\theta(\tau)$  of the deformed fringe on the recording medium can be expressed as:

$$\tilde{\varphi}_\theta(\tau) = 2\pi \frac{\tilde{\tau}}{b} \quad (23)$$

Accordingly, the Gladstone-Dale relation can be combined with the constant  $K$ :

$$\tilde{n}(x, y) = K(\rho(x, y) - \rho_b) \quad (24)$$

and Eqs. (21)~(23) yield the two-dimensional density field in a cross-section perpendicular with respect to a fixed streamwise location  $z$  of the jet as follows:

$$\rho(x, y) = \rho_b + \frac{\lambda_0}{bK} \int_0^\pi \left\{ \int_{-\infty}^{\infty} |\zeta| \mathcal{F}(\tilde{\tau}) \exp(2\pi i \tau \zeta) d\zeta \right\}_{\tau=-x \sin \theta + y \cos \theta} d\theta \quad (25)$$

This equation can be expressed in alternative form with the convolution theorem as follows:

$$\rho(x, y) = \rho_b + \frac{\lambda_0}{bK} \int_0^\pi [k(\tau)^* \tilde{\tau}]_{\tau=-x \sin \theta + y \cos \theta} d\theta \quad (26)$$

where

$$k(\tau) \equiv \mathcal{F}^{-1}(|\zeta|) = \int_{-\infty}^{\infty} |\zeta| \exp(2\pi i \tau \zeta) d\zeta \quad (27)$$

and the symbol  $*$  denotes convolution between  $k(\tau)$  and  $\tilde{\varphi}_\theta(\tau)$ .

Therefore, with the use of Eq. (25) and the Fourier transform method for phase shift analysis [21], the two-dimensional density fields at various streamwise locations  $z$  can be stacked together to form the three-dimensional density field in an asymmetric shock-containing jet.

As shown in Fig. 1, the test nozzle is installed inside a pulley with a gear ratio of 1:4 and it can be rotated around its longitudinal axis at intervals of 5 deg from a rotation angle of  $\theta = 0$  deg to 180 deg via a stepping motor with a gear ratio of 1:36 connected through a timing belt. Therefore, multiview interferograms of a rectangular underexpanded microjet are taken by a complementary metal oxide semiconductor (CMOS) camera (the imaging source, DFK72BUC02), which records a JPEG RGB image (8 bits each color) at a resolution of 2952 × 1944 square pixels.

Fig. 6(a) illustrates a representative interferogram of a rectangular underexpanded microjet, captured at a nozzle pressure ratio (NPR) of 4.0 and an angle ( $\theta$ ) of 0°. This image was taken from the major-axis direction (x-axis direction), with the downstream distance from the nozzle exit as the  $z$ -axis and the vertical upward direction as the  $y$ -axis. The units of the numerical values in Fig. 6(a) are in millimeters. The direction of the wavefront of the background interference fringe is perpendicular to the  $z$ -axis. Enlarged views of Parts A and B, enclosed by blue squares in Fig. 6(a), are shown in Fig. 6(b) and (c), respectively. When there is no flow from the nozzle, uniform interference fringes with a spacing of  $b$  between the fringes appear throughout the field of view, as shown in Fig. 6(b). On the other hand, when there is flow, the interference fringes deform as shown in Fig. 6(c). The displacements of the interference fringes in Fig. 6(c) are not symmetrical with respect to the jet centerline ( $z$ -axis) because the fringes on both sides of the jet centerline always shift in the same direction. For example, if a fringe at a point above the jet centerline moves upward, the fringe at a point symmetrically located below the centerline also moves upward by the same amount. However, when the direction of the wavefront of the background interference fringes is set parallel to the jet centerline, symmetrical fringe movement occurs across the jet centerline. These details are described in [20].

Interferograms similar to Fig. 6(a) are taken by varying the  $\theta$  in 5-deg intervals up to 180 deg and saved as JPEG files, and then turns into an HSV image (8 bits each color) according to the hue ( $H$ ), saturation ( $S$ ), and value ( $V$ ) color models. Interferogram images of microjets are composed of intensity distributions represented by a single parameter  $V$  with an 8-bit grayscale image or 256 different possible intensities. To reduce the amount of data obtained in the experiment, we assumed that the structure of the microjet is symmetrical about  $x$  and  $y$  axes. The spatial resolution ( $\Delta s$ ) and fringe interval ( $b$ ) of the present Mach-Zehnder interferometer are 4.62 μm and 31 μm in the physical plane,

respectively, which can be evaluated based on the physical and image dimensions of the test nozzle. Therefore, a wave corresponding to one wavelength in the intensity distribution of the interferograms can be constituted only around 7 data points ( $b/\Delta s = 6.7$ ) when compared to the 256 (8 bit) grayscale level. Hence, the present MZT system has a high dynamic range for the fringe-shift analysis.

It should be noted that in underexpanded jets, strong shocks predominantly appear near the jet's central axis, causing abrupt density changes in the flow direction. Consequently, if the background interference fringes are aligned with the shock front, the fringes across the shock may collapse, adversely affecting phase extraction. To mitigate this issue, in the present experiment, the background interference fringes were oriented perpendicular to the jet's central axis. Several studies have reported successful phase unwrapping with sufficient accuracy in regions including shocks. For instance, Sugawara et al. [22] effectively reconstructed the axisymmetric density field of an underexpanded microjet containing a Mach disk using Takeda et al.'s method [21]. Similarly, Léon et al. [23] applied Herráez et al.'s technique [24] to successfully reconstruct the instantaneous asymmetric density field of a screeching underexpanded jet in helical mode. In this study, we adopted Herráez et al.'s method [24] for phase unwrapping.

#### 4. Numerical methods

The structures of shock-containing microjets issuing from a rectangular convergent nozzle with an aspect ratio of 10 at the exit face are numerically investigated via the commercial computational fluid dynamics (CFD) software ANSYS Fluent Version 16.0. The flow field of a rectangular microjet emerging from the test nozzle used in the experiment shown in Fig. 2 is numerically reproduced. The center on the nozzle exit plane is taken as the origin, i.e.,  $x = y = z = 0$ , where  $x$  and  $y$  denote the major-axis and minor-axis directions, respectively, and where  $z$  shows the streamwise direction. An image of the whole computational domain is shown in Fig. 7(a). In addition, images of the computational grids on the cross sections of the nozzle exit and near the nozzle exit in the minor-axis plane are shown in Fig. 7(b) and (c), respectively.

The pressure-based compressible RANS equations are numerically solved. Menter's SST $k - \omega$  turbulence model is employed because Sugawara et al. [20,22]) reported that RANS simulations with this turbulence model for round shock-containing microjets are in good quantitative agreement with experimental density fields captured via Mach-Zehnder interferometry. The NPR is held constant at 4.0 where  $p_{os}$  and  $p_b$  are 400 kPa and 100 kPa, respectively, and the plenum temperature  $T_{os}$  upstream of the nozzle is specified at 300 K. The dry air is assumed to follow the perfect gas law with a constant specific heat ratio of  $\gamma = 1.4$ , and the coefficient of viscosity is calculated via Sutherland's formula.

The solid walls including the nozzle wall are treated as adiabatic and no-slip, and all the boundaries except for the left boundary are pressure outlets (i.e.,  $p_b$  is specified). The structured mesh is generated by the mapped face meshing function equipped with ANSYS Fluent, and the total mesh count is approximately 41 million elements with 41 million node points. The grid spacing within a region of  $-1.5 \text{ mm} \leq x \leq 1.5 \text{ mm}$ ,  $-150 \mu\text{m} \leq y \leq 150 \mu\text{m}$  and  $0 \text{ mm} \leq z \leq 10 \text{ mm}$  is relatively uniform and fine ( $10 \mu\text{m}$ ) to resolve the complex shock cell structures. Inside the nozzle, the grid size smoothly decreases in the perpendicular direction with respect to the wall surface to capture the boundary layer. The size of the lowest grids near the nozzle wall surface is approximately  $10 \mu\text{m}$ , which corresponds to 0.8 in terms of the nondimensional variable  $y^+$ . To capture the fine structures of the shock-containing jets accurately, we set the minimum mesh interval to  $10 \mu\text{m}$  in the vicinity of the nozzle exit. In addition, to accurately capture the streamwise development of shear layers originating from the lipline at the nozzle exit, the grid is refined in the direction perpendicular to the lipline, as illustrated in Fig. 7(b). However, to minimize the total

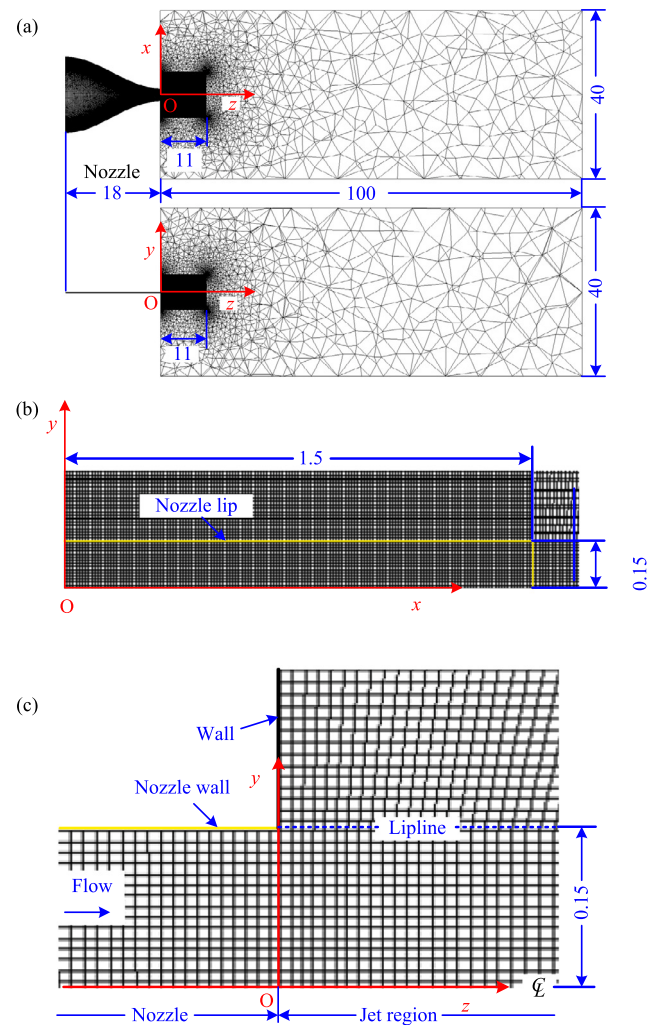


**Fig. 7.** Image of the computational domain and the Cartesian coordinate system ( $x, y, z$ ) with its origin at the center of the nozzle exit plane. All dimensions are in mm. (a) The whole computational domain, (b) the cross-section including the nozzle exit plane, and (c) the zoom view of the computational domains across the nozzle exit at the minor axis plane.

number of grid cells, the grid is coarser in other regions, particularly in the upper right corner of Fig. 7(b).

In the present simulations, fine, medium and coarse grids were created for grid sensitivity analysis and each grid was used to solve the flow field of the rectangular underexpanded microjet. Specifically, the coarse and fine grids were approximately twice and half the size of the medium grid with a minimum grid spacing of  $10 \mu\text{m}$ , respectively. As a result, the grid size has little effect on the density distributions along the liplines in both the minor-axis and major-axis planes. However, a slight influence of the grid size on the density values at the maxima and minima was observed in the density distribution along the jet centerline. Furthermore, we confirmed that the RANS prediction with medium grid resolution can predict the flow field in reasonable agreement with the experimental data. Hence, the medium grid size was selected in the present study to save the computing resources and time.

The CFL number is set on the basis of the pseudo transient under-relaxation method. The UPWIND-type finite volume schemes with the van Albada limiter are used to achieve second-order accuracy in space. The spatial gradients of the flow variables are calculated in a pre-processing step at all vertices via a Green-Gauss approach and then averaged to obtain these gradients at the cell faces when computing viscous

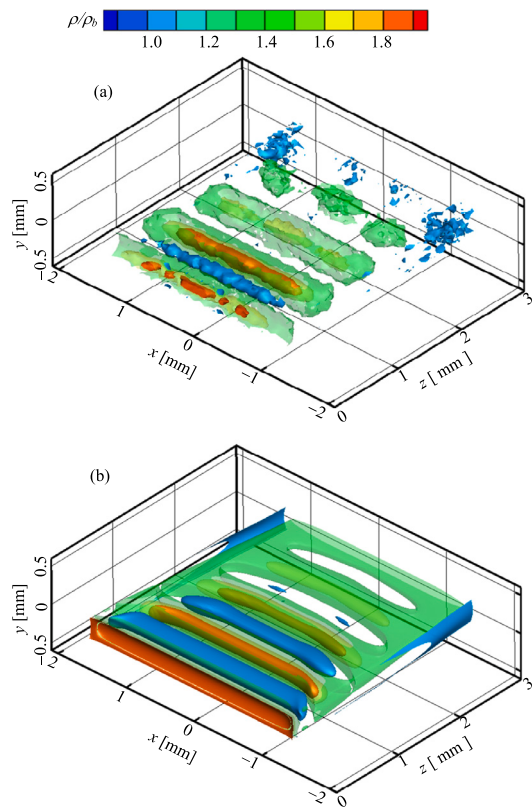


**Fig. 8.** Comparison between the (a) experimental and (b) simulation results for the isopycnic surface of the rectangular microjet with an AR of 10. The density fields are normalized by the ambient density.

fluxes along the edges. For time-integration, the three-stage Runge-Kutta method is used. We iterate the solution sufficiently enough so that the residuals of all equations reduce by an order of three, indicating that the solution shows convergence.

## 5. Results and discussion

### 5.1. Density fields

The three-dimensional density fields of rectangular underexpanded microjets are illustrated in Fig. 8(a) and (b) via isopycnic surfaces for the experiment and simulation. The density fields are normalized by the ambient density  $\rho_b$  and the level of the density is shown at the top of the figure as a color bar.  $x$  and  $y$  denote the major-axis and minor-axis directions, respectively, and  $z$  is the streamwise distance measured from the center of the nozzle exit surface. The spatial evolution of the underexpanded microjets for the experiment and simulation can be clearly observed in Fig. 8(a) and (b). The expansion and compression regions in the rectangular microjet, which are viewed in blue and red, respectively, remain nearly two-dimensional near the nozzle exit, but soon show pronounced three-dimensionality.

The density contour plots in the minor-axis and major-axis planes of the microjet are shown in Fig. 9(a) and (b) with the flow from left to right. The upper and lower halves of each figure show the experimental and numerical results, respectively. The liplines are indicated by white lines parallel to the abscissa. Notably, these figures show the density values on the cross-section including the central axis of the microjet, but not those integrated along the line-of-sight direction. Therefore, they are very useful for verification via direct comparisons with other measurement techniques or numerical codes. As shown in Fig. 9(a), the flow feature of the microjet in the minor-axis plane is clearly different

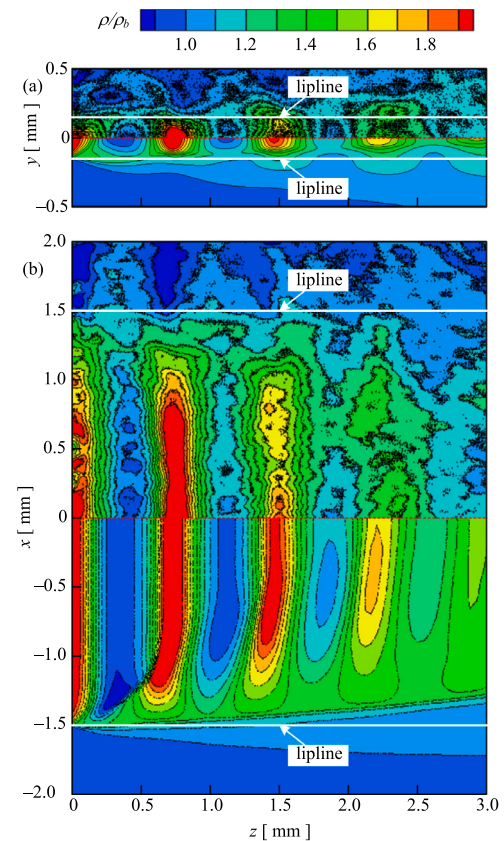


**Fig. 9.** Comparisons between the experimental and simulation results for the density contour plots in the (a) minor-axis plane and (b) major-axis plane. The white lines parallel to the abscissa denote the lipline ( $x = 0$  and  $y = 0.15$  mm) in the minor-axis plane and the lipline ( $y = 0$  and  $x = 1.5$  mm) in the major-axis plane.

from that of an underexpanded microjet emerging from a round convergent nozzle. Recent experimental studies on round underexpanded microjets for  $NPR = 4.0$  have demonstrated the occurrence of a Mach disk within the first shock-cell ([22,25]). However, the presence of a Mach stem, which corresponds to a Mach disk in the case of round jets, cannot be identified in Fig. 9(a).

Fig. 9(b) shows that the geometrical shapes of the first expansion and compression regions agree relatively well between the experimental and simulation results. For the density field after the second shock-cell, the agreement is not as good. The shock wave in the first shock-cell is not discontinuous but has some width in the flow direction. In addition, it has a structure that is nearly straight outward from the jet center axis and bends slightly upstream near the jet lipline. The compression region in the second shock-cell in the experiment has a discrete structure. In contrast, the simulation results indicate that the transverse length of the straight part of the compression region is shorter for downstream shock-cells.

### 5.2. Streamwise density profiles

Three streamwise density profiles inside the rectangular underexpanded microjet including the jet central axis ( $x = y = 0$ ), the lipline ( $x = 0$  and  $y = 0.15$  mm) in the minor-axis plane, and the lipline ( $y = 0$  and  $x = 0.15$  mm) in the major-axis plane are shown in Fig. 10 for the experiment and simulation. The locations of these three characteristic lines are depicted by the white lines in Fig. 9(a) to (c). Each experimental density profile is represented with the uncertainty error where the error contains the precision error only, but not the bias error since it is negligibly small when compared to the precision error

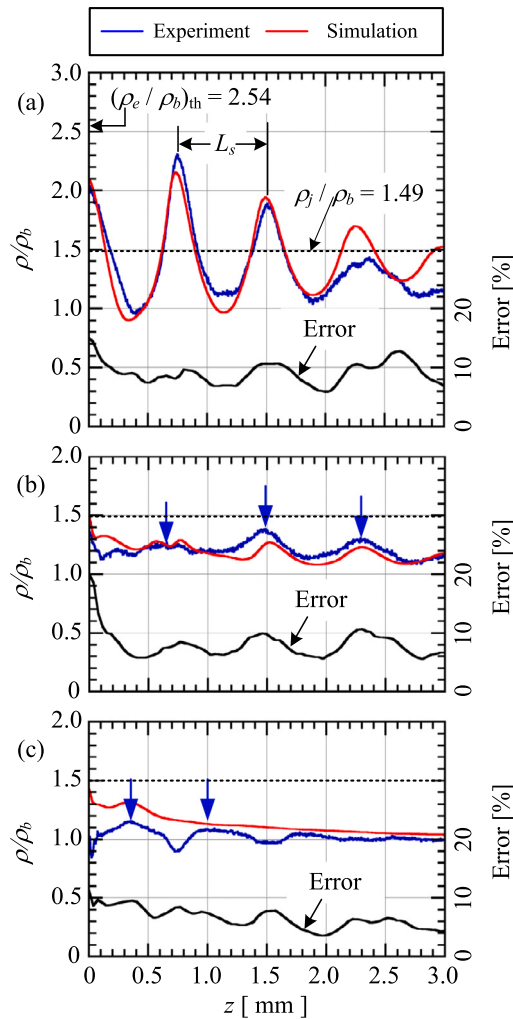


**Fig. 10.** Comparisons between the experimental and simulation results for the streamwise density profiles along the (a) jet centerline ( $x = y = 0$ ), (b) lipline ( $x = 0$  and  $y = 0.15$  mm) in the minor-axis plane, and (c) lipline ( $y = 0$  and  $x = 0.15$  mm) in the major axis plane. The positions of these three distinctive lines are illustrated by the white lines in Fig. 9(a) to (c). The blue and red lines represent the experimental and simulation results, respectively. The black solid line in each figure indicates the uncertainty error of the density non-dimensionalized by  $\rho_b$ .

for density fields of shock-containing jets [17,22]. The precision error  $S$  for the sample of  $N$  measurements ( $N = 5$  for the present experiments) can be calculated by

$$S = \sqrt{\frac{\sum_{i=1}^N (\rho_i - \hat{\rho})^2}{N(N-1)}} \quad (28)$$

with  $\hat{\rho} = \sum_{i=1}^N \rho_i / N$ . The uncertainty error  $U$  for the 95% confidence interval is defined as  $U = t_{95}S$  [26] where  $t_{95}$  is obtained from the student's  $t$ -distribution as  $t_{95} = 2.78$  for  $N = 5$ .

Fig. 10(a) shows a comparison between the experimental and simulation density profiles along the jet central axis. The experimental density profile shown by the blue solid line has an average uncertainty error of  $\pm 9.4\%$ . The numerical result corresponding to the experiment is shown in Fig. 10(a) with the red solid line. The theoretical value at the nozzle exit ( $z = 0$ ), assuming an isentropic change in flow from the nozzle inlet to the exit, is indicated by the leftward arrow with  $(\rho_e / \rho_b)_{th} = 2.54$  where the condition is imposed such that the Mach number at the nozzle exit plane is generally unity for convergent nozzle flows. The fully expanded jet density [22] ( $\rho_j / \rho_b = 1.49$ ) normalized by the ambient density is expressed by the dashed line parallel to the abscissa.

Note that the fully expanded jet pressure  $p_j$  is the same as the back pressure  $p_b$  [22]. The error distribution exhibits periodic fluctuations along the flow direction, with a marked increase at the density distribution maxima. These maxima closely correspond to the locations of shock formation. Furthermore, the error variation is significantly more pronounced at the downstream shock locations compared to the upstream ones, primarily due to the pronounced influence of flapping oscillations [27,28] inherent to rectangular jets.

The densities at the nozzle exit for the experiment and simulation are in good quantitative agreement with each other, but well below the theoretical value. The flow outside the boundary layer from the nozzle inlet to the exit can be assumed to be an isentropic change. Therefore, the freestream Mach number at the nozzle exit can be estimated as  $M_{e\infty} = 1.26$ , using the experimental density value. The reason why the freestream Mach number at the nozzle exit exceeds unity can be explained by the concept of compound choking [29], as described in Section 5.3.

The experimental and numerical densities in Fig. 10(a) decrease rapidly to a minimum value well below  $\rho_j / \rho_b$  because the expansion waves are generated from the nozzle exit lip and then rise sharply above  $\rho_j / \rho_b$  in the compression region by the first shock. The flow Mach number  $M_1$  at the end of the expansion region or the beginning of the compression region in the first shock-cell can be estimated as  $M_1 = 1.96$  using  $\rho_1 / \rho_b = 0.957$  for the experiment, assuming the isentropic flow from the nozzle inlet to the end of the expansion region. Furthermore, if an increase in density from the first minimum to the maximum of the density distribution is attributed to a Mach stem, a combination of the  $M_1$  and the Rankine-Hugoniot relation gives the density ratio just after a normal shock as  $\rho_2 / \rho_b = 2.49$ . This predicted density value exceeds the maximum density value inside the first shock-cell in Fig. 10(a). Thus, the density increase in the first shock cell is not caused by a normal shock or a Mach stem, but by a series of compression waves or weak oblique shock waves. This is also indicated by the fact that the density increase is gradual rather than discontinuous. Density variations similar to those inside the first shock-cell are quasi-periodically repeated downstream to form the second and third shock-cells. The experimental and simulated density profiles are in good quantitative agreement, except downstream of  $z = 2$  mm. The discrepancy between the experimental and simulation results at the downstream locations is considered to be due to the effects of the dynamic motion of the third shock-cell in the flapping mode [30].

A comparison of the experimental and simulated results for the density profile along the lipline in the minor-axis plane is shown in Fig. 10(b) where the experiment has an average uncertainty error of  $\pm 7.8\%$ . The streamwise locations of the density maxima in the experimental density profile are indicated by the blue downward arrows. As shown in a comparison with Fig. 9(a), the density maxima appear at the locations of the outer edges of the compression regions. The error distribution of the density profile along the lipline in the minor-axis plane exhibits a peak at the shock generation locations, analogous to the behavior observed along the central axis of the jet. Furthermore, the magnitude of this peak increases progressively downstream.

A comparison similar to Fig. 10(b) is shown in Fig. 10(c) for the density profile along the lipline in the major-axis plane. The experimental density profile has an average uncertainty error of  $\pm 6.2\%$ . The density profile along the lipline in the major-axis plane varies gradually in the flow direction because as shown in Fig. 9(b), the density along the lipline in the major-axis plane is not affected by the compression regions since they are far enough from the lipline. The simulated density profile along the lipline in the minor axis plane quantitatively captures the experimental waveform. While along the lipline in the major axis plane, it is in excellent agreement with the experimental values except just downstream of the nozzle exit. The error distribution associated with the density profile along the lipline in the major-axis plane peaks near the shock generation locations.

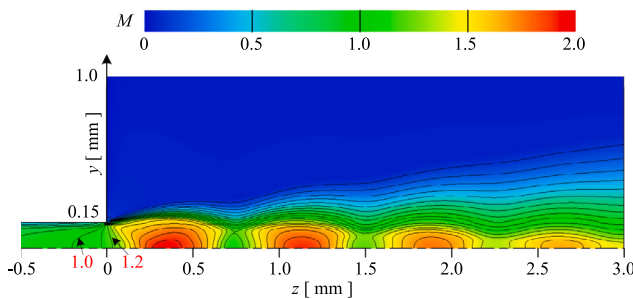


Fig. 11. Simulated Mach number contour plot across the nozzle exit in the minor-axis plane.

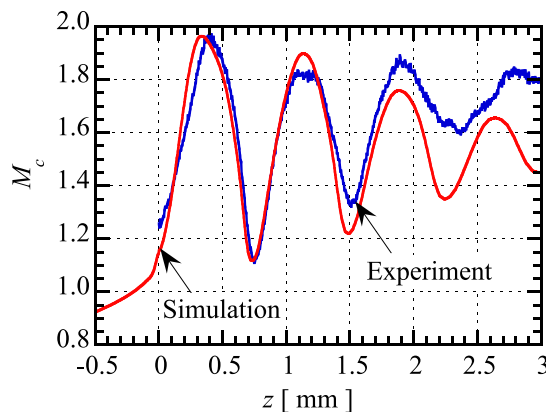


Fig. 12. Comparison between the (a) experimental and (b) simulation results for the streamwise Mach number profile along the jet centerline.

However, due to the diminished influence of the shocks, the overall error decreases progressively downstream.

As shown in Fig. 10(a), the shock-cell spacing  $L_s$  can be defined as the streamwise length between the first and second maxima in the density profile along the central axis of the jet ([25,31]). From Fig. 10(a), the experimentally determined dimensionless shock-cell spacing is  $(L_s/h)_{ex} = 2.56$ . On the other hand, for underexpanded jets issuing from a rectangular nozzle with a design Mach number  $M_d$  and a sufficiently large aspect ratio at the exit, the shock-cell spacing according to the vortex sheet model [32] is given by

$$\frac{L_s}{h} = 2 \left( M_j^2 - 1 \right)^{\frac{1}{2}} \left[ \frac{2 + (\gamma - 1)M_j^2}{2 + (\gamma - 1)M_d^2} \right]^{\frac{\gamma+1}{2(\gamma-1)}} \frac{M_d}{M_j} \quad (29)$$

where  $\gamma$  is the specific heat ratio and where  $M_j$  is the fully expanded jet Mach number, which depends on the NPR as follows:

$$M_j = \sqrt{\frac{2}{\gamma - 1} \left( \text{NPR}^{\frac{\gamma-1}{\gamma}} - 1 \right)} \quad (30)$$

Since our experiment utilizes a convergent nozzle with  $\text{NPR} = 4$ , the theoretical value of  $(L_s/h)_{th}$  is 2.92 when  $M = 1$  in Eq. (29). The Mach number at the nozzle exit can be predicted to be 1.26 instead of 1. With  $M_d = 1.26$  instead of  $M_d = 1$ , the theoretical shock-cell length obtained from Eqs. (29) and (30) is 2.78. That is, the theoretical value is close to the experimental value.

### 5.3. Compound choking

In the theory of one-dimensional isentropic flow through a convergent nozzle, the flow Mach number at the nozzle exit never exceeds unity. However, a nonuniform velocity distribution at the exit of a

convergent nozzle results in an exit Mach number greater than 1 [29]. Kubo et al. [33] experimentally investigated the effects of boundary layers or wall frictions on the freestream Mach number at the nozzle exit of a round convergent nozzle. They clarified the effects of the boundary layer on the Mach number at the nozzle exit plane where a long pipe of four different lengths with a constant cross-sectional area was connected at the exit of a round convergent nozzle. They concluded that if the velocity distribution at the exit of the convergent nozzle is nonuniform due to the boundary layer effect, the freestream Mach number at the exit plane is greater than unity and increases with increasing boundary layer thickness.

The simulated Mach number contour plot across the nozzle exit in the minor-axis plane is shown in Fig. 11 for the positive  $y$  range. The flow direction is from left to right. The numeric values on the contour lines denote the Mach numbers. The contour line with a Mach number of 1 is located upstream of the nozzle exit and has a convex shape on the upstream side. The Mach number along the center axis of the nozzle reaches unity near  $z = -0.25$  mm upstream of the nozzle exit and accelerates downstream, exceeding 1.1 at the exit. In general, the boundary layer developing along the wall inside the nozzle increases in the flow direction. However, the wall boundary layer immediately upstream of the nozzle exit is expected to become thinner due to the effect of expansion waves from the nozzle exit lip. As a result, a state similar to the geometric throat occurs inside the nozzle and the flow Mach number exceeds unity at the nozzle exit. The phenomenon of the Mach number exceeding unity at the exit of a convergent nozzle was also reported by Han et al. [34], who used a two-dimensional rectangular microduct with a height of 500  $\mu\text{m}$  and width of 2,500  $\mu\text{m}$ , and the number density distributions along the duct centerline were measured via the laser-induced fluorescence (LIF) technique.

The Mach number distribution along the central axis of the nozzle in Fig. 11 shows as a red solid line in Fig. 12. In addition, assuming that the flow along the central axis of the nozzle varies isentropically from the plenum chamber upstream of the nozzle to far downstream of the nozzle exit, the Mach number can also be calculated from the experimental density distribution in Fig. 10(a), as shown by the blue solid line in Fig. 12. The Mach number at the nozzle exit already exceeds 1 for both the experiment and simulation and increases with increasing distance in the flow direction to a maximum value of approximately 2. Immediately downstream, the Mach number decreases in the flow direction and reaches a minimum value, but never reaches a subsonic value. In addition, the experimental and simulated Mach number distributions agree very well quantitatively from the nozzle exit to the end of the second shock-cell; this means that the assumption of isentropic flow is correct, i.e. there is no Mach stem or strong shock wave in the jet. For the simulated and experimental Mach number distributions, the maxima and minima gradually decrease and increase, respectively, in the flow direction, but the Mach numbers remain supersonic in the range of the measurements.

For underexpanded microjets emerging from a round convergent nozzle, Tashiro et al. [25] proposed an experimental relation between the maximum Mach number  $M_1$  and the nozzle pressure ratio NPR given by

$$M_1 = 1 + 0.72 (\text{NPR} - 1.89)^{0.76} \quad (31)$$

The theoretical Mach number calculated via Eq. (30) for  $\text{NPR} = 4$  is 2.27, which is 16% higher than the experimental value of 1.96; this is because the fact that compound choking causes the exit Mach number to exceed 1, making the static pressure at the nozzle exit close to the back pressure, thus weakening the degree of underexpansion. This effect also leads to an isentropic change in the flow in the mainstream portion of the jet.

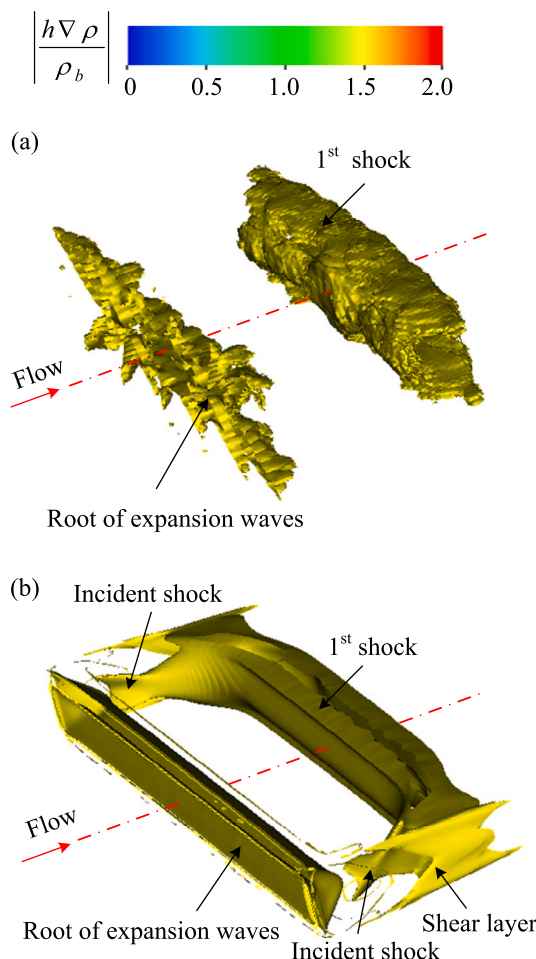


**Fig. 13.** Comparison between the (a) experimental and (b) simulation results for the streamwise evolution of a shock-system in the first shock-cell.

#### 5.4. Shock structures and topology

Shock structures and topology such as the spatial evolution of shock waves, shock-to-shock interactions, shock reflection and diffraction, can be expressed quantitatively via the magnitude of the density gradient vector given by

$$\frac{D_{eq}}{\rho_b} |\nabla \rho| = \frac{D_{eq}}{\rho_b} \sqrt{\left( \frac{\partial \rho}{\partial x} \right)^2 + \left( \frac{\partial \rho}{\partial y} \right)^2 + \left( \frac{\partial \rho}{\partial z} \right)^2} \quad (32)$$

in nondimensional form. It indicates the degree of compression and expansion in every direction. This representation highlights the shock shapes and location of the onset of the expansion waves [22].

Fig. 13(a) shows the three-dimensional structure of the weak shock inside the first shock-cell as well as the root of expansion waves issuing from the nozzle exit lip as evaluated from the experimental density field. The flow direction is indicated by the red dotted line in the figure. The strength of the shock or expansion wave is indicated by the color bar at the top of the figure. Fig. 13(b) shows the numerical results corresponding to the experiment.

The root of the expansion wave has a complex three-dimensional structure in the experiment but a smooth shape in the numerical calculation. In addition, the shear layer, which cannot be confirmed experimentally, can be clearly observed in the numerical results. The first shock has an upward convex structure with some width, but there are no incident shocks as seen in a previous study [35] of a free jet emerging from rectangular convergent nozzles with ARs of 2 and 4. The

numerical results clearly reveal that the incident shock is just inside the shear layer in the major-axis plane. The difference between the experimental and numerical results is unknown in this stage and needs to be verified by other experimental methods.

#### 6. Conclusions

Near-field flow features of an underexpanded microjet emerging from a rectangular convergent nozzle with AR = 10 were experimentally and numerically investigated via the MZT with the finite-fringe setting and the RANS prediction with the SST $k - \omega$  turbulence model.

An isopycnic surface of the rectangular microjet was presented to capture the three-dimensional structure visually. In addition, the density contour plots in the minor-axis and major-axis planes and the density distributions along the three representative characteristic lines, including the jet centerline and the liplines in the minor-axis and major-axis planes, were used to clarify the spatial shape and size of the compression and expansion regions to form the shock-cell structure.

Despite the flow through a convergent nozzle, the freestream Mach number at the nozzle exit exceeds unity owing to the effects of wall frictions, and the location where the flow Mach number is unity exists just upstream of the nozzle exit, which leads to a smaller degree of underexpansion; consequently, no Mach stem occurs inside the first shock-cell, instead, weak shocks are produced. As a result, the flow field from the nozzle inlet to the location of the end of the second shock-cell obeys the isentropic process.

Shock structures and topology are displayed with the magnitude of the density gradient vector for the first time. The structure of the weak shock inside the first shock-cell shows a convex shape upstream. Incident shocks from the nozzle lip are not visible in the experiment, but are generated in the simulation just inside the jet shear layers in the major-axis plane.

#### CRediT authorship contribution statement

**Shota Yoshimi:** Writing – original draft, Visualization, Validation, Software, Investigation, Formal analysis, Data curation. **Takahiro Yamashita:** Software. **Shinichiro Nakao:** Supervision, Resources, Project administration, Investigation, Conceptualization. **Yoshiaki Miyazato:** Writing – review & editing, Supervision, Conceptualization.

#### Funding

This work was supported in part by Grants-in-Aid for Scientific Research(C) (Grant Nos. 20K04272 and 20K04290).

#### Declaration of competing interest

The authors declare that they have no known competing financial interests or personal relationships that could have appeared to influence the work reported in this paper.

#### Acknowledgments

The authors are deeply grateful to Tenta Tashiro of the University of Kitakyushu for his help in adjusting the Mach-Zehnder interferometer. The authors would also like to thank Dr. Takeshi Miyaguni of the University of Kitakyushu for the fabrication of the test nozzle.

#### Data availability

The data that support the study findings are available from the corresponding author upon reasonable request.

## References

- [1] Y.H. Kweon, H.D. Kim, Study on the wiping gas jet in continuous galvanizing line, *J. Therm. Sci.* 20 (2011) 242–247.
- [2] D.K. Lee, D.N. Jeong, T.K. Ahn, N.G. Park, Precursor engineering for a large-area perovskite solar cell with > 19% efficiency, *ACS Energy Lett.* 4 (2019) 2393–2401.
- [3] J.X. Zhong, W.Q. Wu, L. Ding, D.B. Kuang, Blade-coating perovskite films with diverse compositions for efficient photovoltaics, *Energy Env. Mater.* 4 (2021) 277–283.
- [4] S. Hu, Q. Shang, P. Zhang, J. Chen, F. Zhang, X. Miao, Study of airflow regime upon optic inside frequency multiplying device and achievement of cleaning technique, *Optik* 240 (2021) 166777.
- [5] H. Kashimura, Y. Masuda, Y. Miyazato, K. Matsuo, Numerical analysis of turbulent sonic jets from two-dimensional convergent nozzles, *J. Therm. Sci.* 20 (2011) 133–138.
- [6] T. Handa, K. Mii, T. Sakurai, K. Immura, S. Mizuta, Y. Ando, Study on supersonic rectangular microjets using molecular tagging velocimetry, *Exp. Fluids* 55 (1725) (2014).
- [7] V.M. Aniskin, A.A. Maslov, I.S. Tsirulnikov, I.V. Timofeev, Visualization of supersonic axisymmetric and plane underexpanded microjets, *J. Flow Vis. Image Process.* 22 (2015) 213–227.
- [8] V.M. Aniskin, A.A. Maslov, S.G. Mironov, I.S. Tsirulnikov, I.V. Timofeev, An experimental study of the structure of supersonic flat underexpanded microjets, *Tech. Phys. Lett.* 41 (2015) 508–510.
- [9] V.M. Aniskin, A.A. Maslov, S.G. Mironov, I.S. Tsirulnikov, I.V. Timofeev, Effect of the pitot microtube diameter on pressure measurement in plane supersonic microjets, *Flow Meas. Instrum.* 70 (2019) 101655.
- [10] T. Handa, Study on the collapse length of compressible rectangular microjets, *Exp. Fluids* 61 (196) (2020).
- [11] S. Yoshimi, S. Nakao, Y. Miyazato, Study of rectangular underexpanded microjets, *Open J. Fluid Dyn.* 13 (2023) 122–131.
- [12] D. Ragni, F. Schrijer, B.W. van Oudheusden, F. Scarano, Particle tracer response across shocks measured by PIV, *Exp. Fluids* 50 (2011) 53–64.
- [13] T. Feng, J.J. McGuirk, Measurements in the annular shear layer of high subsonic and under-expanded round jets, *Exp. Fluids* 57 (2016) 1–25.
- [14] K.B. Yüceil, A comparison of PIV and interferometric Rayleigh scattering measurements in the near field of underexpanded sonic jets, *Aerospace Sci. Technol.* 67 (2017) 31–40.
- [15] F. Nicolas, D. Donjat, O. Léon, G. Le. Besnerais, F. Champagnat, F. Micheli, 3D reconstruction of a compressible flow by synchronized multi-camera BOS, *Exp. Fluids* 58 (2017) 1–15.
- [16] R. Fukunaga, M. Ezoe, S. Nakao, Y. Miyazato, Application of rainbow schlieren tomography for shock-containing rectangular jets, *J. Vis.* 25 (2022) 687–695.
- [17] T. Nagata, T. Sakashita, S. Nakao, Y. Miyazato, Three-dimensional flow features of underexpanded jets emerging from an elliptic convergent nozzle, *Exp. Fluids* 65 (146) (2024).
- [18] A.J. Smits, T.T. Lim, *Flow visualization: techniques and examples*, Imperial College Press, 2000.
- [19] S. Yagi, S. Inoue, S. Nakao, D. Ono, Y. Miyazato, Optical measurements of shock waves in critical nozzles at low Reynolds numbers, *J. Flow Control. Measur. Vis.* 5 (2017) 36–50.
- [20] S. Sugawara, S. Nakao, Y. Miyazato, Y. Ishino, K. Miki, Quantitative flow visualization of slightly underexpanded microjets by Mach-Zehnder interferometers, *Flow Turbul Combust* 106 (2021) 971–992.
- [21] M. Takeda, H. Ina, S. Kobayashi, Fourier-transform method of fringe-pattern analysis for computer-based topography and interferometry, *J. Opt. Soc. Amer. A* 72 (1982) 156–160.
- [22] S. Sugawara, S. Nakao, Y. Miyazato, Y. Ishino, K. Miki, Three dimensional reconstruction of a microjet with a Mach disk by Mach-Zehnder interferometers, *J. Fluid Mech.* 893 (A25) (2020).
- [23] O. Léon, D. Donjat, F. Olchewsky, J.M. Desse, F. Nicolas, F. Champagnat, Three-dimensional density field of a screeching under-expanded jet in helical mode using multi-view digital holographic interferometry, *J. Fluid Mech.* 947 (A36) (2022).
- [24] M.A. Herráez, D.R. Burton, M.J. Lalor, M.A. Gdeisat, Fast two-dimensional phase-unwrapping algorithm based on sorting by reliability following a noncontinuous path, *Appl. Opt.* 41 (2002) 7437–7444.
- [25] T. Tashiro, R. Fukunaga, D. Utsunomiya, S. Nakao, Y. Miyazato, Y. Ishino, Flow features of underexpanded microjets emerging from a round convergent nozzle, *Exp. Fluids* 64 (55) (2023).
- [26] H.W. Coleman, W.G. Steele, *Experimentation, Validation, and Uncertainty Analysis for Engineers*, John Wiley & Sons, 2018.
- [27] E. Gutmark, K.C. Schadow, C.J. Bicker, Near acoustic field and shock structure of rectangular supersonic jets, *AIAA J.* 28 (1990) 1163–1170.
- [28] G. Raman, Cessation of screech in underexpanded jets, *J. Fluid Mech.* 336 (1997) 69–90.
- [29] A. Bernstein, W.H. Heiser, C. Hevenor, Compound-compressible nozzle flow, *J. Appl. Mech.* 34 (1967) 548–554.
- [30] S. Kajii, N. Nishijima, Pressure field around a rectangular supersonic jet in screech, *AIAA J.* 34 (1996) 1990–1996.
- [31] T. Nagata, M.M. Islam, T. Miyaguni, S. Nakao, Y. Miyazato, Shock-cell spacings of underexpanded sonic jets emerging from elliptic nozzles, *Exp. Fluids* 63 (111) (2022).
- [32] C.K.W. Tam, The shock-cell structures and screech tone frequencies of rectangular and non-axisymmetric supersonic jets, *J. Sound Vib.* 121 (1988) 135–147.
- [33] K. Kubo, Y. Miyazato, K. Matsuo, Study of choked flows through a convergent nozzle, *J. Therm. Sci.* 19 (2010) 193–197.
- [34] B. Han, Y. Matsuda, Y. Egami, T. Handa, Investigation on choking behavior of gas flow in microducts, *Microfluid. Nanofluid.* 22 (122) (2018).
- [35] N. Menon, B.W. Skews, Shock wave configurations and flow structures in non-axisymmetric underexpanded sonic jets, *Shock Waves* 20 (2011) 175–190.